Available online at www.sciencedirect.com
ScienceDirect
Journal of Photochemistry and Photobiology A: Chemistry 196 (2008) 143–153
Journal of Photochemistry and Photobiology A:Chemistry
www.elsevier.com/locate/jphotochem

Synthesis of ZnO–carbon composites and imprinted carbon by the pyrolysis of $ZnCl_2$-catalyzed furfuryl alcohol polymers

Federico Cesano, Domenica Scarano *, Serena Bertarione, Francesca Bonino, Alessandro Damin, Silvia Bordiga, Carmelo Prestipino [1], Carlo Lamberti, Adriano Zecchina

Nanostructured Interfaces and Surfaces (NIS), Centre of Excellence, Department of Chemistry IFM, University of Turin, Centre of Reference INSTM, Via P. Giuria 7, I-10125 Torino, Italy

Available online 6 August 2007

Abstract

Porous ZnO–carbon composites were produced from homogeneous mixtures of furfuryl alcohol–$ZnCl_2$. $ZnCl_2$, acting as a Lewis acid, promotes the polymerization of furfuryl alcohol at low temperatures (60–70 °C). Upon gradually increasing the temperature, using a N_2 atmosphere containing ~1000 ppm O_2, from 80 °C to 600 °C the viscous matrix is transformed into a black solid, in which Zn(II) is dispersed. The sample treated at 600 °C is covered by an uniform layer of ZnO microcrystals that are embedded in the carbonaceous matrix. The underlying carbon support contains a distribution of holes, whose size and shape is related to the shape of the ZnO microcrystals. Further heating in the 600–800 °C range leads to the disappearance of the ZnO phase, which after reduction to volatile Zn, leaves a pure carbon film that retains the original pores. The use of an inorganic Lewis acid as a precursor of a highly volatile metal, which acts as templating agent for the pores in the resulting carbon, is a novel result. If the thermal treatments in the 80–800 °C interval are conducted in vacuo, the formation of the ZnO phase is not observed.

Keywords: ZnO–carbon composites; Microporous carbon; Morphology; Structure; Optical properties

1. Introduction

Microporous carbons (MCs) have attracted a great attention in recent years due to the wide applicability to many fields, including catalytic supports, gas storage, molecular sieves, porous membranes and electrodes. Porous carbons are usually prepared by pyrolysis of suitable polymers in vacuum or in controlled atmosphere under inert gas flow. Polyacrylonitrile (PAN), phenolic resin, polyimides, poly(*p*-phenylene vinylene), polyvinyl acetate and polyfurfuryl alcohol (PFA) are the most commonly used precursors [1–8]. When compared to other precursors, PFA (obtained by acid-catalyzed polymerization of the monomer) provides a relatively high carbon yield. The formed carbon phase shows distinct microporosity and is characterized by the presence of defects such as pentagons, heptagons, vacancies, impurities and other non-hexagonal rings [7,9,10]. PFA-derived carbons show bottle-like nano- and micropores, with narrow opening connected to larger voids. Their size distribution is dramatically affected by pyrolysis conditions. The presence of pores of different sizes and shapes is evidenced by X-ray scattering (pores with 25–35 Å pore diameters) and by selective adsorption of molecular probes with increasing size (pores with 3.8–4.8 Å range) [1].

The catalysts promoting the polymerization of furfuryl alcohol (FA) commonly reported in literature are (i) mineral acids (H_2SO_4, etc.) [8,11–13], (ii) organic acid (*p*-toluenesulphonic, etc.) [8,14,15], (iii) acid zeolites (HY, HZSM5) [16,17] and (iv) (I_2, $SnCl_4$, $TiCl_4$) [18–20]. In this study we have investigated the catalytic effect of a Lewis acid ($ZnCl_2$) on the polymerization of FA and the fate of the catalysts dispersed in the polymeric matrix upon thermal treatments in the 80–800 °C interval under N_2 controlled atmosphere. To this purpose PFA resins have been first obtained by dissolving known quantities of $ZnCl_2$ (Lewis

* Corresponding author. Tel.: +39 011 6707834; fax: +39 011 6707855.
E-mail addresses: federico.cesano@unito.it (F. Cesano), domenica.scarano@unito.it (D. Scarano), serena.bertarione@unito.it (S. Bertarione), francesca.bonino@unito.it (F. Bonino), alessandro.damin@unito.it (A. Damin), carmelo.prestipino@esrf.fr (C. Prestipino), carlo.lamberti@unito.it (C. Lamberti), adriano.zecchina@unito.it (A. Zecchina).
[1] Current address: ESRF, BP 220, F-38043 Grenoble, France.

1010-6030/$ – see front matter © 2007 Elsevier B.V. All rights reserved.
doi:10.1016/j.jphotochem.2007.07.033

acid catalyst) in liquid FA at room temperature. By stirring the mixture under mild conditions (80 °C) a rapid polymerization of FA with subsequent formation of a brown, highly viscous phase of PFA is observed. Of course, during this phase, $ZnCl_2$ (or its hydrolysis products) remains dispersed into the polymeric matrix.

These results are interesting for three main reasons. The first one is related to the catalytic activity of $ZnCl_2$ in furfuryl alcohol polymerization, which is an observation never reported before. The second one is related to the controlled synthesis of ZnO–carbon composites, characterized by a uniform layer of highly dispersed ZnO crystallites implanted on the surface of the carbon matrix. This method could be extended to the synthesis of other oxide–carbon composites possessing photocatalytic properties [21,22] and finding application (for example) in wastewater treatments for photodegrading organic pollutants [23] and bacteria photodeactivating [24,25]. The third reason is related to the formation, for high pyrolysis temperatures, of a pure carbon phase containing holes whose distribution and size is driven by the Zn content.

2. Experimental

2.1. Synthesis

PFA resin has been obtained by stirring solutions of $ZnCl_2$ in FA (4.8 wt.%, 9 wt.% and 17 wt.%) at 80 °C for several hours. The resulting viscous PFA composite containing $ZnCl_2$ (or its hydrolysis products) was then treated at 100 °C, 200 °C, 400 °C, 600 °C and 800 °C under N_2 gas flow (100 ml/min). In our experiments the N_2 gas was deliberately contaminated with O_2 (1000 ppm), because this greatly enhances the formation of a surface layer of ZnO (see below). The vital role of small amounts of oxidizing agents in the gas phase (O_2, H_2O and CO_2 formed during the carbonization process) for the formation of a layer of ZnO is confirmed by the fact that by performing the thermal treatments in vacuo (i.e. in absence of O_2) the formation of ZnO is not observed.

2.2. Characterization

To control the polymerization mechanism, the structure of the carbon phase and the fate of $ZnCl_2$, ZnO and Zn during the thermal treatments, the samples containing the lowest Zn percentage (4.8 wt.%) were characterized, after each thermal treatment, by means of several techniques (EXAFS, XANES, XRD, Raman, AFM, SEM, TPD and volumetric adsorption measurements). The samples containing 9% and 17% Zn were only characterized by SEM, AFM and volumetric measurements.

X-ray absorption experiments at the Zn K-edge were performed at the BM29 beamline at the European Synchrotron Radiation Facility (ESRF) [26]. The monochromator was equipped with two Si(3 1 1) flat crystals and harmonic rejection was achieved using Rh-coated mirrors after monochromator. The adopted experimental set-up allows a direct energy/angle calibration for each spectrum avoiding any problem related to little energy shifts due to small thermal instability of the monochromator crystals [27]. For the XANES part a sampling step of 0.3 eV has been applied while, for EXAFS parts a constant sampling step in k-space ($\Delta k = 0.025$ Å^{-1}) has been used. For each sampled point an integration time of 3 s has been used.

The crystallinity of the samples have been estimated by *XRD analysis* (X-ray diffractometer with Cu Kα radiation with X-ray beam at $\lambda = 0.154$ nm, using a standard Bragg–Brentano geometry).

Raman spectra have been recorded at room temperature by using: (i) Renishaw Micro-Raman System 1000 with He/Cd laser operating at 442 nm and at 325 nm; (ii) Renishaw Raman Microscope with diode laser operating at 785 nm; (iii) Renishaw Micro-Raman System 1000 connected to a HVSCA (high-vacuum structural and chemical analyzer supporting the 514 nm laser excitation wavelength and fitted to a JEOL JSM-6060LV SEM).

Diffuse reflectance UV–vis spectra have been recorded directly on the material at room temperature by means of a Varian spectrometer (UV-Vis-NIR Cary 5) equipped with a diffuse reflectance attachment.

The morphology of the sample has been investigated by means of SEM (Leica Cambridge Stereoscan 420 instrument equipped with an energy dispersive X-ray spectroscopy) and AFM (Park Scientific Instrument Auto Probe LS) microscopies.

N_2 adsorption–desorption experiments have been carried out at 77 K (Micromeritics ASAP 2010 instrument) to determine the Brunauer–Emmett–Teller (BET) surface area and micropore volume (t-plot method); before the surface area determination the samples were always outgassed at 400 °C for 12 h.

Temperature programmed desorption (TPD) analysis (Hyden Catlab) have been performed in bar mode (pressure ranging in the 10^{-6} to 10^{-8} Torr range) to evaluate the evolution of the volatile species and hydrocarbons (H_2O, CO, CO_2, CH_4, C_2H_4, C_3H_8) formed during PFA thermal decomposition, from room temperature to 800 °C (5 °C/min heating rate), under He gas flow (50 ml/min). Results concerning TPD analyses are reported in Supporting information.

3. Results and discussion

3.1. The effect of thermal treatments on the concentration and local structure of ZnO as studied by X-ray absorption

XANES and EXAFS spectroscopies on the Zn K-edge are suitable to investigate the evolution of the structure of Zn in the carbon phase and a complete series of measurements have been planned and performed on samples characterized by an initial 4.8 wt.% Zn concentration. In Fig. 1a the normalized XANES spectra obtained after treatments under controlled atmosphere at 100 °C, 200 °C, 400 °C, 600 °C and 800 °C are reported (bottom part). In the top part of the same figure the spectra of model materials (Zn, ZnO and $ZnCl_2$) are also reported for comparison. In Fig. 1b and c the corresponding modulus and imaginary part of k^3-weighted phase uncorrected FT of the EXAFS signals are reported.

The XANES and EXAFS data give information on four different aspects: concentration of the adsorbing species, valence

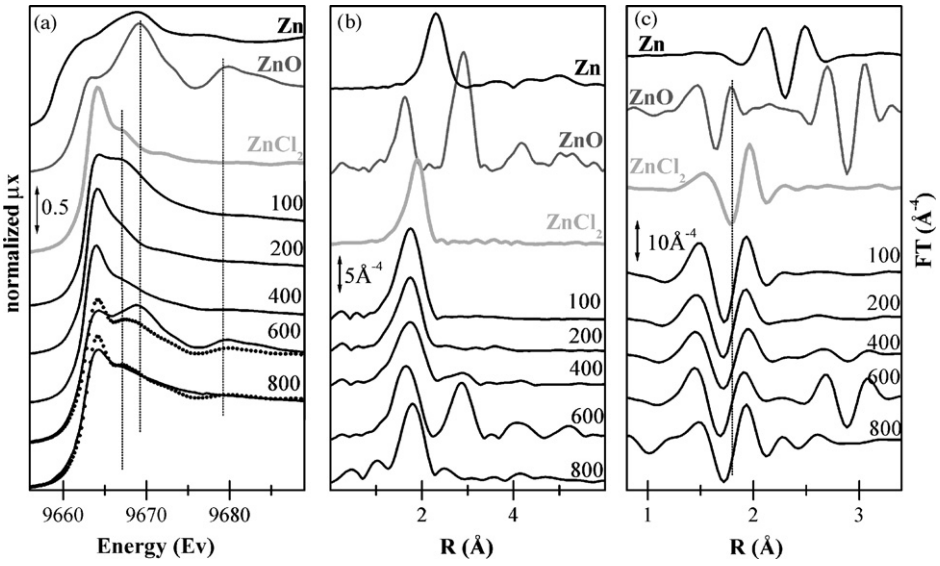

Fig. 1. (a) Normalized XANES edges. (b and c) k^3-weigthed, phase uncorrected Fourier transformation of the EXAFS signals, modulus and imaginary part, respectively. On the top of the figures, the model compound spectra (metal Zn, $ZnCl_2$ and ZnO) are reported from the top to the bottom, whereas on the bottom the spectra of the composite materials, obtained under different temperatures of pyrolysis (100 °C, 200 °C, 400 °C, 600 °C, 800 °C, respectively) are compared.

state, surrounding ligands and local structure. In particular being the edge jump of the XANES proportional to the total amount of Zn on the sample, information about the evolution of the Zn concentration upon the thermal treatment can be obtained.

The first important conclusion deriving from our measurements is that the concentration of Zn is substantially constant in the 100–400 °C interval, while it decreases of about 50% and 90% for the samples treated at 600 °C and 800 °C, respectively (Table 1, last column). We ascribe the disappearance of Zn from the composite for treatment temperatures in the 400–800 °C range, to the reduction of the Zn(II) precursor ($ZnCl_2$ or ZnO) present in the carbon matrix with formation of Zn, which being volatile at this *T*, quickly leaves the composite as vapor (see below).

At this point the following questions arise: (a) which is the evolution of $ZnCl_2$ catalyst dissolved into the polymeric matrix during the thermal treatments in the 80–400 °C range?; (b) does the reduction product of the catalysts (starting at about 400 °C) become dissolved into the carbonaceous matrix before leaving the sample as vapor?; (c) does the process of Zn oxidation occur by oxygen or with other oxidants, leading to formation of ZnO with a purely surface process or does it involve Zn dissolved into the bulk (if any)?

To answer these questions it is useful to make at first a few general considerations on the XANES features of model compounds (Fig. 1a, top part):

(a) Metallic Zn exhibits the first absorption feature in the XANES at 9661 eV (shoulder), which occurs at an energy value distinctly lower than that of Zn(II) compounds ($ZnCl_2$ and ZnO), and a broad feature at 9669 eV. ZnO is characterized by a better resolved shoulder at 9663.5 eV, by a strong and sharper absorption at 9669 eV (see vertical marker), followed by a deep minimum at 9676 eV and by a second important feature at 9680 eV (see vertical marker).
(b) $ZnCl_2$ exhibits a sharp absorption maximum at 9664 eV, followed by an almost monotonic decrease interrupted by a weak feature at 9667 eV (see vertical marker).

On the basis of these considerations we can conclude that, as a small fraction of metal phase inside a majority of oxidized phases could be easily detected by XANES spectroscopy [27,28], we can safely rule out a significant fraction of Zn metal remains dissolved into the samples (whatever is the thermal treatment). This implies that, if Zn(0) is formed by reduction of Zn(II) during the high-temperature treatments, it does not accumulate into the carbon matrix and leaves immediately the composite in form of vapor [29] so explaining the Zn loss determined by the edge jump value.

The XANES spectra of the sample pyrolyzed at 200 °C and 400 °C exhibit features very close to those of $ZnCl_2$ model compound. This strongly suggests that $ZnCl_2$ catalyst remains

Table 1
Quantitative data extracted from the X-ray absorption spectra of the samples pyrolyzed at increasing temperatures

Pyrolysis *T* (°C)	Fit of the XANES spectra		Edge jump
	ZnO phase relative fraction	$ZnCl_2$-like phase relative fraction	Total Zn fraction
100	0.04 ± 0.03	0.96 ± 0.03	1.0
200	−0.01 ± 0.01	1.01 ± 0.01	1.0
400	0.06 ± 0.01	0.94 ± 0.02	1.0
600	0.31 ± 0.03	0.69 ± 0.03	0.5
800	0.20 ± 0.02	0.80 ± 0.01	0.1

Relative fraction of the $ZnCl_2$ and ZnO phases as obtained from the fit of the XANES spectra. Fraction of total amount of Zn on the sample (relative to the sample pyrolyzed at 100 °C) as obtained from the evaluation of the edge jump. The reported error bars are the statistic ones; intrinsic errors of the technique, related to the determination of the relative phase fractions are reasonably ±10%.

dissolved as such into the matrix for treatments at temperatures lower than 400 °C.

The fingerprint features of ZnO at 9669 eV and 9676 eV are clearly visible in the XANES spectrum of the sample treated at 600 °C (see vertical markers) in presence of oxidizing contaminants. As usually done with XANES spectra of samples containing different phases [30,31] the relative fraction of the Zn atoms having a $ZnCl_2$- and a ZnO-like local environment has been determined performing a linear fit of the spectra of the two model compounds. Results, summarized in Table 1, indicate that the local environment of Zn is that of $ZnCl_2$ for all samples pyrolyzed up to 200 °C. Treatment at 400 °C results in the appearance of a small (6%), but appreciable, fraction of ZnO, that becomes important in the sample fluxed at higher temperatures: 31% and 20% of the total Zn fraction actually present at 600 °C and 800 °C, respectively (see Table 1).

The quantitative results extracted from the XANES spectra are fully supported by a qualitative investigation of the k^3-weighted, phase uncorrected FT of the EXAFS signal. The modulus of the FT of model compounds (Fig. 1b, top part) are characterized by the following features: (i) Zn metal exhibits a Zn–Zn first shell contribution at 2.30 Å; (ii) ZnO has a first shell Zn–O contribution at 1.63 Å, a very strong second shell Zn–O–Zn signal at 2.91 Å and higher shells contributions at 4.18 Å, 5.03 Å and 5.30 Å; (iii) $ZnCl_2$ exhibits a first shell Zn–Cl signal at 1.91 Å. For all samples, the first shell peak of the samples is close to that of Zn–Cl, however, due to the rather broad character of this contribution, nothing more specific can be said. The second shell Zn–O–Zn at 2.91 Å, typical of the ZnO phase, starts to be appreciable after pyrolysis at 400 °C, becoming strong in the sample treated at 600 °C, where also the higher shells contribution around 4 Å and 5 Å are clearly visible. The presence of the high shell contributions is the clear evidence of the high crystallinity of this phase. For this sample the first shell peak is markedly shifted to lower *R*-values, reflecting the relatively higher contribution of the Zn–O signal. This picture fully agrees with the quantitative XANES analysis. The straightforward agreement ends for the sample treated at 800 °C, where we need to assume an amorphization of the remaining 20% of the ZnO phase, to account for the disappearance of the higher shells contribution. Note however that this fraction represents only 2% of the total Zn initially present in the material. Consequently the accuracy of the EXAFS datum is therefore questionable.

Much more informative is the imaginary part of the FT (Fig. 1c). As the first shell Zn–O and Zn–Cl contributions are almost in an opposition of phase in a large k range, the imaginary part of the Zn–O signal in ZnO has a maximum at 1.78 Å (see vertical marker), where that of Zn–Cl signal in $ZnCl_2$ has a minimum, being its maximum at 1.97 Å (see vertical marker). This means that the imaginary part of the FT is highly sensitive in the discrimination between Zn–Cl and Zn–O contributions. All samples, whatever is the treatment temperature, clearly show an imaginary part of the FT which is, in the 1.0–2.3 Å region, very close to that of $ZnCl_2$ model compound, reflecting the dominating role played by the Zn–Cl bonds. This qualitative picture is in full agreement with the quantitative XANES results (see Table 1).

In conclusion the main results deriving from this analysis can be summarized as follows:

(a) In samples treated in the 80–400 °C interval the composite can be described in terms of $ZnCl_2$ dissolved in an amorphous carbonaceous matrix.
(b) Starting from 400 °C a ZnO phase starts to appear, whose concentration reaches a maximum around 600 °C an than strongly declines at 800 °C.
(c) The Zn concentration is constant in the 100–400 °C interval and then declines for higher treatment temperatures. In the samples treated at 800 °C the concentration of Zn is ∼10% of the starting one.
(d) Zn phase is never observed.

3.2. The evolution of the crystalline structure of the ZnO–carbon composites upon thermal treatments: XRD results

From the XAS data discussed above, it has been inferred that the sample treated at 600 °C is characterized by a decrement of the total Zn concentration and by the formation of a ZnO phase, while the sample treated at 800 °C is characterized by ∼10% concentration of Zn and disappearance of the ZnO phase. In order to support these findings and gain information on the structure of the carbon matrix, the X-ray diffraction patterns of the 4.8 wt.% sample treated at 600 °C (curve a) and 800 °C (curve b), respectively have been investigated and the results are reported in Fig. 2 together with the graphite and ZnO standard XRD reflections.

The XRD pattern of the sample obtained at 600 °C reveals two broad diffraction peaks, with maxima at 24.5° and 43.3° and narrow peaks at 31.7°, 34.4°, 36.2°, 47.5° and 56.5°. The two broad peaks are assigned to the (0 0 2) and (1 0 0) diffraction peaks of turbostratic carbon phases [32]. From the (0 0 2) peak of the carbon phase, the value of d_{002} interlayer spacing (3.647 Å) and the apparent crystallite size along the c axis, d (1.6 nm) can be obtained. Both figures are in agreement with literature data of turbostratic carbons [33,34]. The narrow peaks are ascribed to the (1 0 0), (0 0 2), (1 0 1), (1 0 2) and (1 1 0) diffractions of ZnO. From the peak broadening and by using Scherrer's equation $d = K\lambda/(\beta \cos\theta)$ [35] (where d is the mean grain size, λ the X-ray wavelength, β the FWHM of the diffraction line, θ means the diffraction angle and K is a constant, which has been assumed to be 0.9), the size of scattering coherent domains have been calculated. In agreement with the procedure adopted by several authors [36] the main grain sizes of the ZnO microcrystals, as obtained from the (1 0 1) direction at 36.2°, are calculated to be ≈130 nm.

The XRD pattern of the sample treated at higher temperature (800 °C) shows only the two broad diffraction peaks typical of a disordered carbon phase without graphitic ordering. This disordered structure, which cannot be substantially modified by a further thermal treatment at 900 °C (data not shown for sake of brevity) is a characteristic feature of the carbon phase derived by pyrolysis of PFA [9,10]. It is a matter of fact that highly graphitic carbons can be obtained at low temperatures (550–900 °C) only

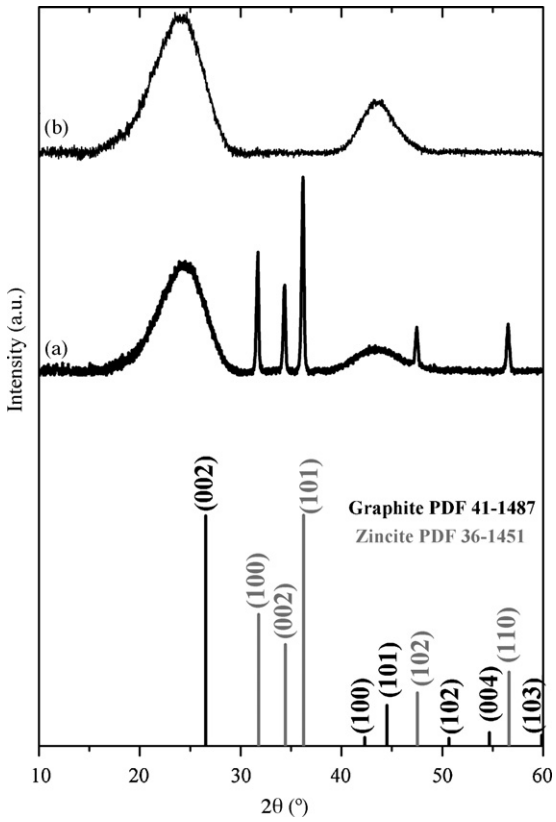

Fig. 2. XRD patterns of the samples obtained from a thermal treatment at 600 °C (a) and at 800 °C (b), respectively. On the bottom the diffraction peaks of standard graphite and wurtzite ZnO are reported.

by the catalytic decomposition of C feedstocks (hydrocarbons, CO) on metal nanoparticles (Ni, Fe, Co) [37,38], which promote the carbon polymerization and graphitization.

In conclusion the XRD patterns confirm that samples treated at 600 °C contain an appreciable amount of well-crystallized ZnO and that this phase disappears upon heating at 800 °C under controlled atmosphere. As far the structure of the carbonaceous support is concerned, it is similar to that of turbostratic carbon obtained by condensation and pyrolysis of furfuryl alcohol in absence of $ZnCl_2$. From this observation it is also inferred that while $ZnCl_2$ is acting as efficient catalyst for alcohol polymerization and carbonization, it is not showing any catalytic activity for subsequent graphitization (unlike Ni, Fe and Co).

3.3. Morphology of microcrystalline ZnO formed on the carbon support as evidenced by SEM

SEM images reported in Fig. 3a–c show different regions of the surface of the sample, treated at 600 °C. This temperature has been chosen because the XANES, EXAFS and XRD data have indicated a substantial formation at this temperature of a ZnO phase.

In particular from Fig. 3a, it is evident that the system is constituted by a carbonaceous support (black part) covered by an almost continuous layer of ZnO microcrystals (white part). The black part, where the carbon support is emerging, is the result of the manipulation during the preparation of the sample for SEM measurements, which has caused the detachment of the film from the substrate.

Of course the size of these black areas is changing from one experiment to the other.

From Fig. 3b it can be deduced that the white regions are fully decorated by a compact and homogeneous layer of randomly oriented ZnO microcrystals, less than 1 μm in size presumably implanted on the carbon matrix, whose terminations are imaged also by AFM (inset of Fig. 3b). AFM topographies also confirm that well-defined single ZnO microcrystals are growing, which expose regular and extended prismatic and hexagonal faces. The SEM analysis of the carbon substrate (Fig. 3c) clearly evidences the presence of holes. As these holes have radii similar to those of the ZnO microcrystals (see also the white spots of Fig. 3c, corresponding to residual ZnO microcrystals still adhering to the substrate), we hypothesize that they correspond to the regions where the ZnO microcrystals were implanted, before being reduced to Zn (which leaves the sample as vapor).

As for the explanation of the mechanism of ZnO layer formation on the sample treated in a flow of nitrogen containing 1000 ppm of oxygen, we think that in the 400–600 °C interval the $ZnCl_2$ catalysts dispersed in the carbonaceous matrix is gradually reduced to Zn, which readily migrates towards the surface, where it is gently oxidized to ZnO. The emerging ZnO microcrystals remain temporarily implanted in the carbonaceous matrix, so contributing to the imprinting of the carbon surface. In other words, ZnO behaves as templating agent of the surface layers of carbon. The vital role of ZnO microcrystals in the imprinting process is demonstrated by the experiment performed in vacuo (Fig. 3d). As a matter of fact, under conditions characterized by the total absence of oxygen and by the fast removal of other impurities with potential oxidizing properties (like CO_2 and H_2O), the formed Zn leaves the solid as vapor without the formation of an intermediate layer of ZnO. Consequently the resulting carbon surface does not show the characteristic holes illustrated in Fig. 3b.

The presence of a ZnO layer is not permanent: as a matter of fact thermal treatments at higher T (even in presence of a small oxygen concentration) favor the final reduction of ZnO to Zn, which leaves the sample as vapor with final formation of a nearly pure carbonaceous material.

This is demonstrated by SEM and AFM images of the samples treated at 800 °C, which do not show any more evidence of the presence of residual ZnO microcrystals (Fig. 4a). Furthermore, they clearly show the imprinted character of the carbon surface, as holes and craters, where the ZnO were implanted, are clearly visible.

It is evident that the SEM and AFM data are in full agreement with XAS and XRD results.

A pictorial representation of the process can be found in Scheme 1, where the main steps of the process are drawn. More in detail, by moving from the first picture, where the Zn(II)/porous carbon composite is shown, which is the major product for temperatures lower than 600 °C, to the second one, which represents the carbonaceous phase covered by a film of ZnO (obtained at 600 °C), we come to the last one, which highlights the formation (at 800 °C) of the pure imprinted

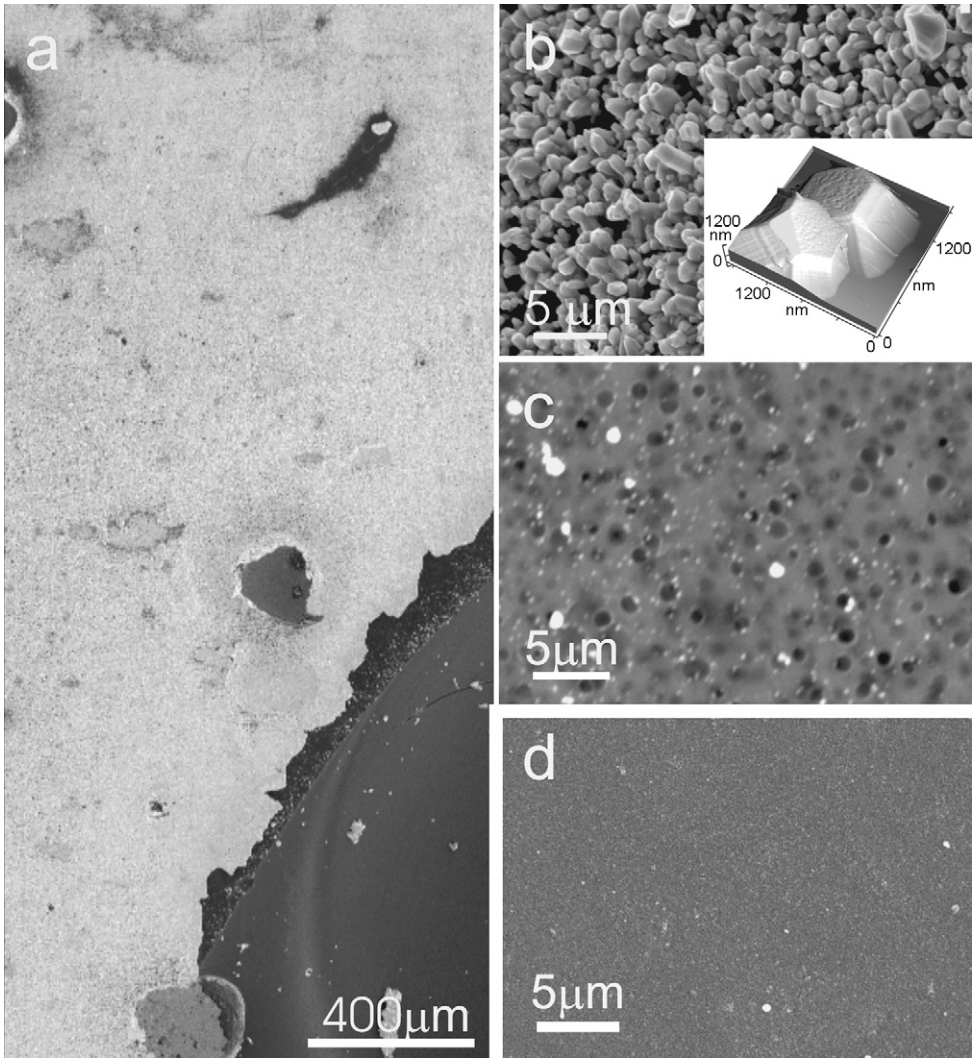

Fig. 3. (a) SEM image of a carbon/ZnO sample obtained after thermal treatment at 600 °C ($ZnCl_2$: 5%, w/w). (b) Enlarged SEM image of randomly oriented ZnO microcrystals grown on the carbon phase, whose terminations are imaged also by AFM (inset bottom right, b). (c) SEM image of the underlying carbon porous matrix, having holes comparable in size with those of the rare ZnO crystals. (d) SEM image of a carbon material obtained under vacuum thermal treatment at 600 °C.

carbon phase characterized by holes, where the ZnO crystallites were previously implanted. Of course we do not exclude that the size of the holes is also partially determined by the consumption of the carbon in direct contact with the ZnO particles.

3.4. Structural properties of the ZnO–carbon composite as studied by Raman spectroscopy

Further support to the morphological results, obtained on the sample treated at 600 °C, comes also from the micro-Raman

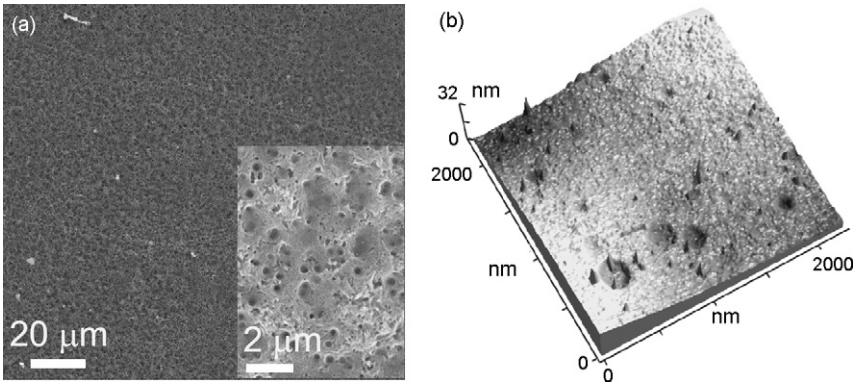

Fig. 4. (a) SEM image of the carbon material obtained from a sample ($ZnCl_2$: 5%, w/w) treated at 800 °C. (b) Enlarged AFM image of a selected area where the random distribution of differently sized pockets is highlighted.

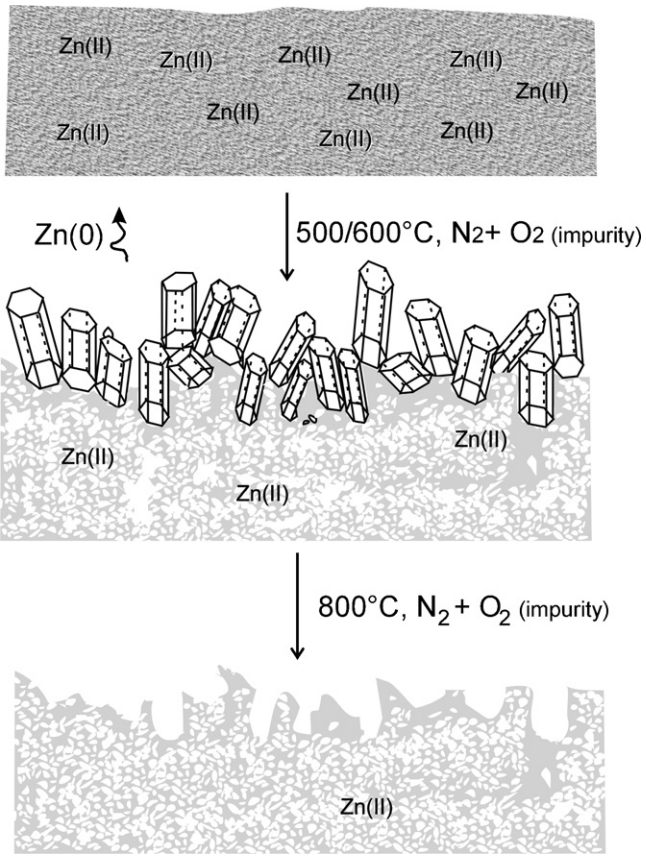

Scheme 1.

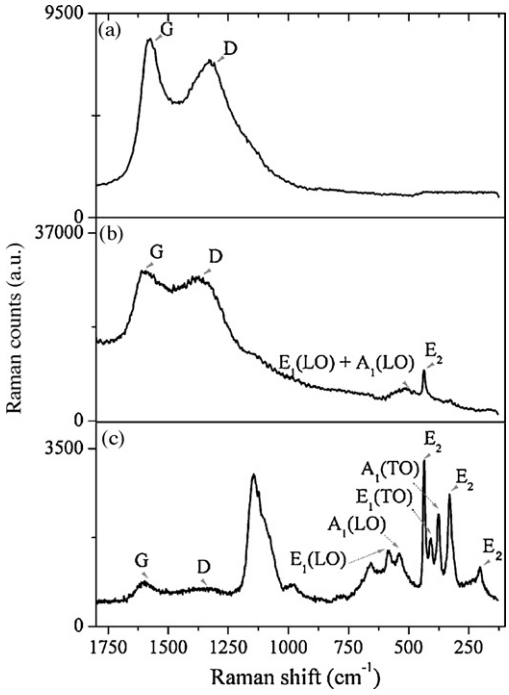

Fig. 5. Micro-Raman spectra, performed with the $\lambda = 514$ nm laser excitation, of the sample obtained at 600 °C: (a) carbon porous matrix, (b) ZnO–Carbon polycrystalline composite and (c) pure ZnO crystals.

spectra, performed with the 514 nm laser excitation wavelength. In Fig. 5a and b the spectra obtained on a ZnO-free region (image of Fig. 3c) and on ZnO-rich region (image of Fig. 3b) of the carbon composite are shown. These spectra are compared with that of pure ZnO microcrystals (Fig. 5c) erased from a carbon surface in a separate experiment.

From the spectrum reported in Fig. 5a two bands of quite similar intensity, are observed at 1580 cm^{-1} and 1350 cm^{-1}. Following the literature [39] the presence of two bands (G and D) of similar intensities is indicative of the presence of a turbostratic carbon phase, rather than of a well-graphitized one. As a matter of fact, in case of standard graphite, the intensity ratio of both bands is greatly different: the G band (always present on highly ordered crystalline sample) is narrow and with high intensities, while the D band is wide with very low intensity (because it is related to disorder) (data not reported for sake of brevity) [40].

In Fig. 5b, besides the G and D carbon bands, previously discussed, also additional modes in the 600–300 cm^{-1} range are observed. The broad and weak features in the 600–500 cm^{-1} range can be assigned to E_1 (LO) and A_1 (LO) longitudinal phonon optical modes of ZnO, while the sharp peak at 436 cm^{-1} is related to the first-order (high) frequency E_2 mode (typical of wurtzite phase). The low intensities of the peaks (compared with those of well-grown ZnO crystals) is indicative of a disordered ZnO phase.

The previous assignment is confirmed by the spectrum reported in Fig. 5c, where the micro-Raman spectrum of larger and well-defined microcrystals erased from the surface in a different experiment, is illustrated. In this spectrum the bands at 585 cm^{-1} (E_1 LO), at 536 cm^{-1} (A_1 LO), at 436 cm^{-1} (E_2 high), at 409 cm^{-1} (E_1 TO), at 377 cm^{-1} (A_1 TO) are associated with the first-order Raman active modes of the ZnO phase, while the intense features at 1200–1050 cm^{-1}, at 332 cm^{-1} and at 205 cm^{-1} are associated with the second-order Raman active modes [41–45].

As already demonstrated in the characterization of different materials [46–54], the use of different laserlines can improve significantly the information extracted from a Raman study. Therefore, to gain more information on the structures of the ZnO layer and of the carbon support, the Raman spectra of samples obtained at 600 °C and at 800 °C, with the whole series of laser beams at 785 nm, 514 nm, 442 nm and 325 nm are compared in Fig. 6a and b.

The spectrum obtained on the 600 °C treated sample (white regions in Fig. 3a) with the 325 nm line is characterized by three bands at about 1750 cm^{-1}, 1150 cm^{-1} and 570 cm^{-1}. These peaks are the first-, second- and third-order Raman active modes of ZnO. When laser frequencies in the 442–785 nm range are used, the spectra of the carbonaceous substrate is fully emerging (G and D bands): this manifestation tends to obscure the Raman modes of ZnO. We can speculate about the reasons, why the 325 nm line is not exciting the Raman modes of carbon, while the higher wavelength lines do. We think that we are in presence of two effects:

(a) The shielding effect of the ZnO, which is larger and more efficient for frequencies near to the absorption edge of ZnO.
(b) The resonance-type response of the carbonaceous phase for $\lambda > 325$ nm.

This is the case, shown by the experiment illustrated in Fig. 5b, where the Raman spectra of the pure carbon phase are reported (see below). It can be observed that the intensities of the G and D bands, low for $\lambda = 325$ nm, reach a maximum for $\lambda = 514$ nm and then decrease.

From the Raman spectra of the samples obtained at 800 °C (Fig. 6b) it can be observed that the relative intensities of the D and G bands are changing with the excitation energies. This information is useful because it contains some structural information. More in detail the ratio of the integrated intensities (I_D/I_G) decreases with increasing laser energy. This result is in agreement with the fact that the high-photon energies are known to reduce the intensity of the D peak [39–45,55]. The observed displacement of the D Raman peak, from 1309 cm^{-1} to 1410 cm^{-1} with increasing laser beam energies, whereas G band remains at 1580 cm^{-1}, is due to a resonant Raman process, where a coupling of the *k*-vector of electronic states involved in the light absorption and the *k*-vector of the plasmons contributing to the Raman spectra is occurring [56]. In other words, since the excitation resonates with the band gap of a particular cluster and selects the corresponding vibration mode, for high-photon energies, smaller clusters having wider band gap become preferentially excited, so causing the associated modes to shift upwards [39,57]. It is also useful to underline that the Raman peaks of specimens treated at 800 °C are slightly narrower with respect to those of the samples treated at 600 °C and that the G/D intensity ratio is moderately increased. This indicates that the samples treated at 800 °C are slightly more graphitic. However they are far from showing a high graphitic order and substantially maintain the original turbostratic character. This result is in full agreement with XRD results.

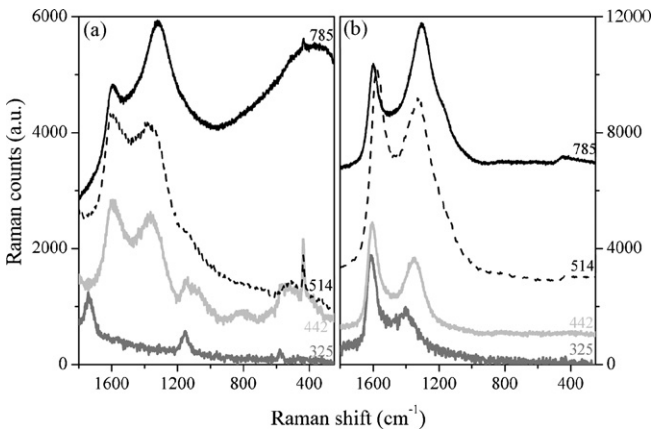

Fig. 6. Raman spectra performed with the whole series of laser beams ($\lambda = 785$ nm, 514 nm, 442 nm and 325 nm) of samples obtained at (a) 600 °C and (b) 800 °C.

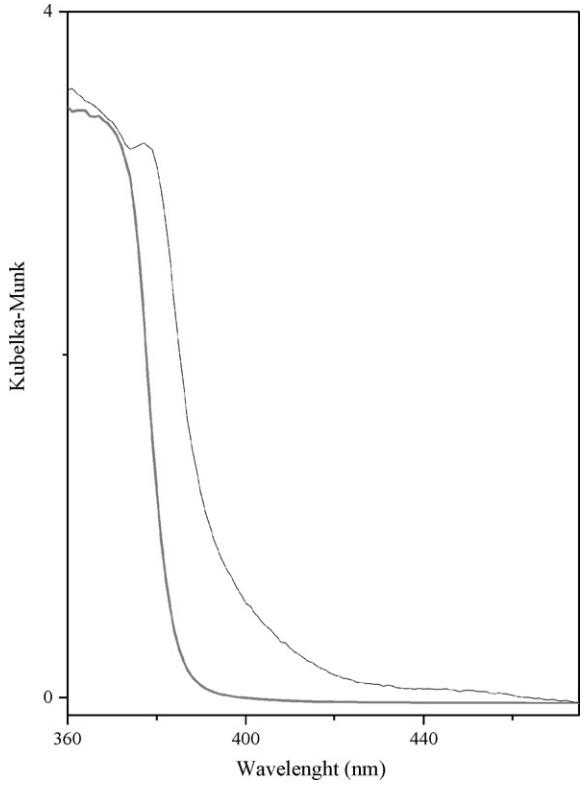

Fig. 7. UV–vis spectra of pure ZnO (Kadox) (gray curve) and ZnO–carbon composite treated at 600 °C (black curve).

3.5. Optical properties of the ZnO–carbon composite: evidence of formation of a ZnO/C-doped phase with potential photocatalytic applications

Fig. 7 shows the UV–vis spectra in the reflectance mode of pure Kadox ZnO (gray curve) and of ZnO–carbon composite treated at 600 °C (black curve). From this figure it is well evidenced that the ZnO–carbon system is characterized by an absorption edge located at a lower frequency value with respect to that of pure Kadox ZnO. The observed red shift is about 10 nm with respect to the 380 nm observed for Kadox. Furthermore ZnO/carbon sample shows weak and broad absorptions at ~430–540 nm, which are absent on pure ZnO. Similar absorptions have been previously reported [58] and have been attributed to oxygen vacancies, because C moved some oxygen on the ZnO phase.

About the observed red shift of the absorption edge, we can hypothesize that C doping into the ZnO lattice can contribute to the formation of impurity states in the band gap and that optical transitions from the impurity states to the conduction band can lead to the red shift of the optical absorption spectrum for the C-doped ZnO.

To our knowledge the problem of the effect of C doping on the optical and conduction properties of ZnO has never been treated theoretically. However theoretical calculations on the effect of other IV group elements (Si, Ge) on the optical properties of ZnO [59] suggest that their presence is associated with appearance of states in the band gap, which could explain the experimental observations.

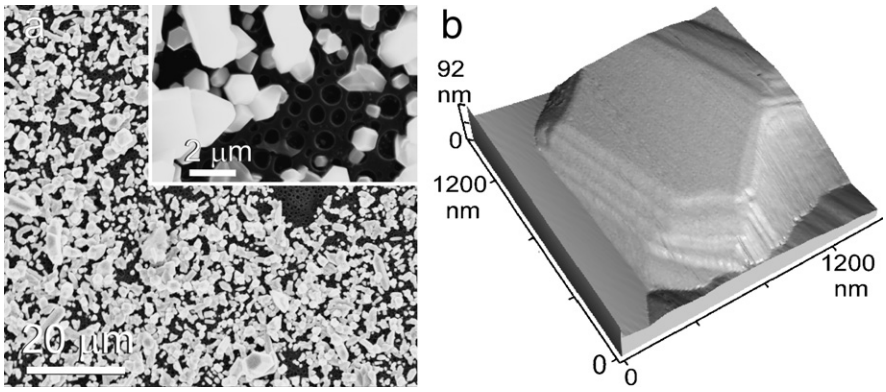

Fig. 8. (a) SEM image of the ZnO–carbon composite material obtained from a sample ($ZnCl_2$: 9%, w/w) treated at 600 °C: in the inset SEM enlarged view of a selected area in (a), where ZnO microcrystals are emerging from a carbon imprinted surface; (b) AFM image of ZnO microcrystals terminations.

In conclusion, the ZnO crystals grown or implanted on a carbon support, following the procedure outlined before, are characterized by novel optical properties, which suggest possible utilization for photocatalytic applications.

3.6. The effect of Zn concentration on the morphology of the ZnO layers and of the carbon substrate

As before discussed, the surface layers of the carbon derived from pyrolysis of a sample containing 4.8% Zn can be imprinted by in situ grown ZnO microcrystals. From this it comes out that an obvious extension of the research was to verify the effect of changing the concentration of $ZnCl_2$ (and hence of Zn) in the precursor sample on the morphology of the imprinted surface. For this reason, samples containing 9 wt.% and 17 wt.% have been treated, following the same procedure illustrated for the 4.8% samples. Following the reasonable assumption that the catalytic polymerization and pyrolysis of these more concentrated samples is not substantially altered, our attention has been mainly focused on the morphological aspects of the transformations.

The SEM and AFM images of samples containing 9 wt.% and 17 wt.% of Zn treated at 600 °C and at 800 °C are illustrated in Figs. 8–11a and b, respectively.

The following items can be summarized:

(i) The surface of samples containing 9% Zn, treated at 600 °C is fully covered by ZnO microcrystals, which have 1–2 μm size and a quite homogeneous extension of regular prismatic and hexagonal faces, as also imaged by the AFM topography of Fig. 8b, where extended terraces can be highlighted. Unlike the sample containing 4.8% Zn, the layer of ZnO is less compact and the microcrystals are less homogeneously oriented. In the regions free from ZnO microcrystals, the underlying structure of the supporting carbon phase is emerging clearly (see also the inset of Fig. 8a). This surface is characterized by a distribution of holes about 1 μm in diameter.

(ii) The presence of holes in the carbon phase is better documented in Fig. 9a and b corresponding to samples treated at 800 °C. As a matter fact in these samples the layer of ZnO microcrystals is no more present, and hence the surface of carbon can be studied without any interference from the ZnO overlayer. Two facts merit special mention: (1) with respect to the 4.8% sample the surface is less smooth and shows signs of fragmentation (Fig. 9a); (2) AFM analysis is very clearly imaging the presence of a distribution of holes with size in the 0.2–0.5 μm range.

(iii) Moving to Fig. 10a and b, corresponding to the sample containing 17% Zn and treated at 600 °C we notice that the ZnO crystals do not form a densely packed array and

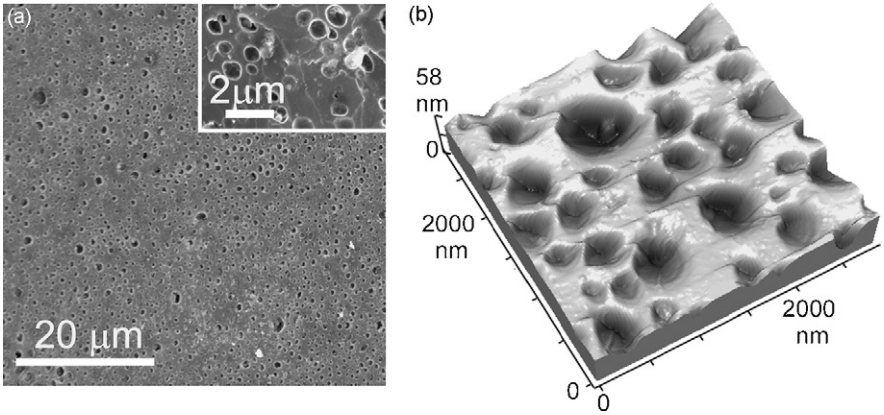

Fig. 9. (a) SEM image of the carbon material obtained from a sample ($ZnCl_2$: 9%, w/w) treated at 800 °C: in the inset SEM enlarged view of a selected area in (a); (b) AFM image of the imprinted carbon surface.

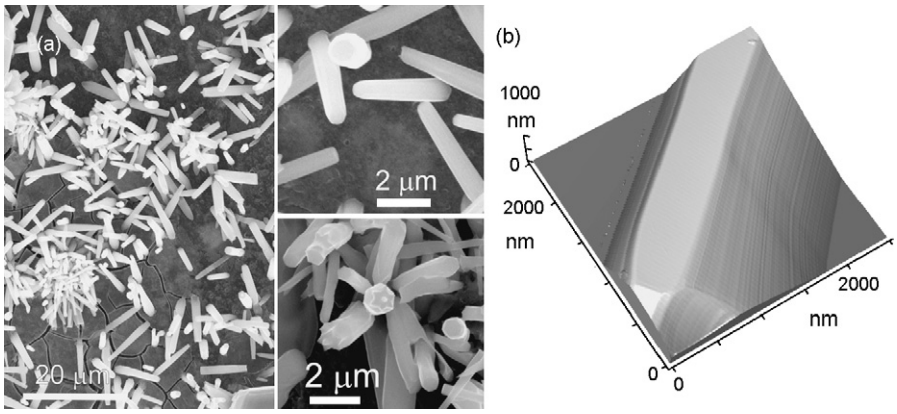

Fig. 10. (a) SEM image of the ZnO–carbon composite material obtained from a sample ($ZnCl_2$: 17%, w/w) treated at 600 °C. (b and c) SEM enlarged views of selected areas where elongated ZnO microcrystals with odd terminations are emerging from the carbon surface. (d) AFM image of the prismatic faces of an elongated ZnO microcrystal.

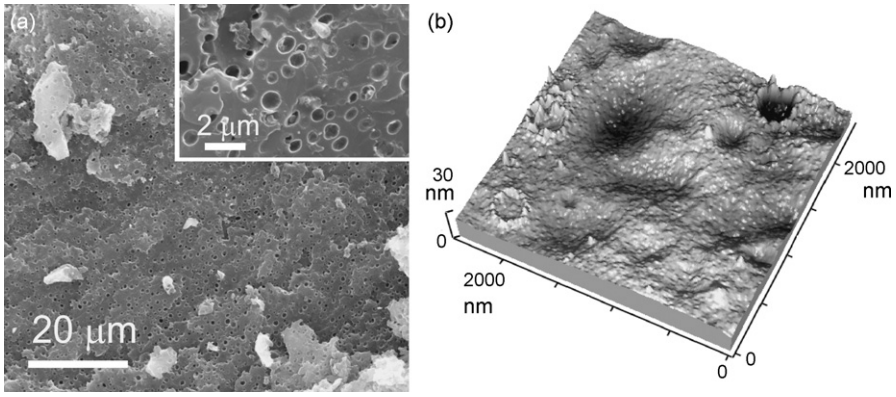

Fig. 11. (a) SEM image of the carbon material obtained from a sample ($ZnCl_2$: 17%, w/w) treated at 800 °C: in the inset a SEM enlarged view of a selected area in (a). (b) AFM image of the imprinted carbon surface.

they are remarkably elongated along the prismatic direction (Fig. 10a). Notice that ZnO microcrystals show, beside a predominant extension of prismatic faces, as also imaged by AFM analysis (Fig. 10b), highly heterogeneous terminations, moving from purely hexagonal faces (on the top right of Fig. 10a) to more complex, star-like shaped facelets (on the bottom right of Fig. 10a). As ZnO microcrystals do not form a compact layer, in Fig. 10a it is possible to see clearly also the underlying carbon surface. We notice that, unlike the previous cases, this surface is full of fractures and the presence of holes is less evident.

(iv) The state of the carbon surface after complete elimination of the ZnO overlayer is illustrated by SEM and AFM images obtained on the sample treated at 800 °C (Fig. 11a and b). From them it is possible to conclude that the surface is highly irregular, as well evidenced from AFM micrograph (see also Fig. 11b) and that the diameter of holes is smaller than observed on more diluted samples.

If the result obtained on the samples containing 4.8 wt.%, 9 wt.% and 17 wt.% Zn are compared, we conclude that: (i) upon increasing the concentration of Zn, the ZnO overlayers become less and less homogeneous; (ii) the carbon surface, although always imprinted (presence of holes) is becoming more and more irregular.

As far the surface area of the supporting carbon phases is concerned, there is a clear evidence of a dependence upon Zn concentration. The measured BET values are comprised in the 288–379 m^2/g interval, the highest value being more progressively observed on the system containing the highest Zn content.

4. Conclusions

Microporous carbons are obtained from a FA–$ZnCl_2$ mixture by pyrolysis under controlled N_2 atmosphere (containing 1000 ppm O_2). The process is constituted by intermediate stages, leading to the initial formation of (i) PFA/Zn(II) composite (through the action of the Zn^{2+} Lewis acid catalyst); (ii) to ZnO–carbon composite and (iii) to a pure carbon phase. For $T < 400$ °C, Zn(II) remains dispersed in the carbonaceous matrix. For T comprised in the 400–600 °C interval, metal Zn is formed and migrates at the surface of the carbon, where by contacting the O_2 impurities it forms a ZnO film characterized by ZnO microcrystals implanted in the carbon matrix. The thickness of the ZnO film is maximum at 600 °C. At higher temperatures (600–800 °C), the ZnO is reduced by the carbon phase and the

formed Zn(0) leaves again the sample as vapor phase. As a result, a pure imprinted carbon phase is generated.

The effect of the $ZnCl_2$ concentration on the process of ZnO and carbon phase formation has been studied in detail. Moving to high Zn content, the morphology of the ZnO microcrystals obtained at 600 °C, is changing from rombohedral shapes, where the relative extension of prismatic and hexagonal faces is quite similar, to more elongated structures, where the growth direction along the prismatic faces becomes predominant. As far as the imprinted carbon phase, it gradually changes from a regular distribution of holes (for low Zn concentration) to a more disordered situation (for high Zn concentration), with wide pockets and small cavities simultaneously present.

Acknowledgements

The authors thank MIUR, INSTM Consorzio and NANOMAT Project for their economical support. The authors would like to thank also Dr. M. Bloomfield (Renishaw Plc, Old Town, Wotto-under-Edge, Glouchestershire GL127DW, UK) for helping in SEM/Raman combined investigations.

Dr. P.L. Solari and whole staff of BM29 beamline of the ESRF are gratefully acknowledged for the friendly and highly competent support during X-ray absorption experiments performed in the frame of proposal CH-1700.

Appendix A. Supplementary data

Supplementary data associated with this article can be found, in the online version, at doi:10.1016/j.jphotochem.2007.07.033.

References

[1] H.C. Foley, Micropor. Mesopor. Mater. 4 (1995) 407.
[2] M. Singh, S.C. Farmer, J. Mater. Sci. Lett. 16 (1997) 946.
[3] S.M. Saufi, A.F. Ismail, Carbon 42 (2004) 241.
[4] M.B. Shiflett, H.C. Foley, Science 285 (1999) 1902.
[5] A.F. Ismail, L.I.B. David, J. Membr. Sci. 193 (2001) 1.
[6] M.S. Strano, A.L. Zydney, H. Barth, et al., J. Membr. Sci. 198 (2002) 173.
[7] H.O. Pierson, H.O. Pierson (Eds.), Handbook of Carbon, Graphite, Diamond and Fullerenes—Properties, Processing and Applications, William Andrew Publishing/Noyes, Park Ridge, NJ, USA, 1993, p. 399.
[8] A.J.G. Zarbin, R. Bertholdo, M. Oliveira, Carbon 40 (2002) 2413.
[9] V. Petkov, R.G. DiFrancesco, S.J.L. Billinge, et al., Phil. Mag. B: Phys. Condens. Matter Stat. Mech. Electron. Opt. Magn. Proper. 79 (1999) 1519.
[10] P.J.F. Harris, A. Burian, S. Duber, Phil. Mag. Lett. 80 (2000) 381.
[11] J.F. Yao, H.T. Wang, J. Liu, et al., Carbon 43 (2005) 1709.
[12] Z.H. Hou, X.H. Li, Z.Q. He, et al., J. Mater. Sci. 39 (2004) 3793.
[13] T. Vergunst, F. Kapteijn, J.A. Moulijn, Carbon 40 (2002) 1891.
[14] M. Principe, P. Ortiz, R. Martinez, Polym. Int. 48 (1999) 637.
[15] M. Sthel, J. Rieumont, R. Martinez, Polym. Test. 18 (1999) 47.
[16] J. Rodriguez-Mirasol, T. Cordero, L.R. Radovic, et al., Chem. Mater. 10 (1998) 550.
[17] M. Kruk, M. Jaroniec, T.W. Kim, et al., Chem. Mater. 15 (2003) 2815.
[18] R. Gonzalez, J.M. Figueroa, H. Gonzalez, Eur. Polym. J. 38 (2002) 287.
[19] R. Gonzalez, J. Rieumont, J.M. Figueroa, et al., Eur. Polym. J. 38 (2002) 281.
[20] M. Choura, N.M. Belgacem, A. Gandini, Macromolecules 29 (1996) 3839.
[21] D. Li, H. Haneda, Chemosphere 51 (2003) 129.
[22] H. Kim, W.M. Sigmund, J. Mater. Res. 18 (2003) 2845.
[23] J. Villasenor, P. Reyes, G. Pecchi, J. Chem. Technol. Biotechnol. 72 (1998) 105.
[24] H.L. Liu, T.C.K. Yang, Process Biochem. 39 (2003) 475.
[25] O. Yamamoto, K. Nakakoshi, T. Sasamoto, et al., Carbon 39 (2001) 1643.
[26] A. Filipponi, M. Borowski, D.T. Bowron, et al., Rev. Sci. Instrum. 71 (2000) 2422.
[27] C. Lamberti, G. Spoto, D. Scarano, et al., Chem. Phys. Lett. 269 (1997) 500.
[28] V. Bolis, S. Maggiorini, L. Meda, et al., J. Chem. Phys. 113 (2000) 9248.
[29] N.N. Greenwood, A. Earnshaw, Chemistry of the Element, 2nd ed., Pergamon Press, Oxford, 1998.
[30] C. Prestipino, S. Bordiga, C. Lamberti, et al., J. Phys. Chem. B 107 (2003) 5022.
[31] C. Lamberti, S. Bordiga, F. Bonino, et al., Phys. Chem. Chem. Phys. 5 (2003) 4502.
[32] D.J. Johnson, C.N. Tison, Br. J. Appl. Phys. (J. Phys. D) 2 (1969) 787.
[33] A. Cuesta, P. Dhamelincourt, J. Laureyns, et al., J. Mater. Chem. 8 (1998) 2875.
[34] A. Tanaka, S.H. Yoon, I. Mochida, Carbon 42 (2004) 591.
[35] L.S. Birks, H. Friedman, J. Appl. Phys. 17 (1946) 687.
[36] Y.G. Wang, S.P. Lau, H.W. Lee, et al., J. Appl. Phys. 94 (2003) 354.
[37] K.P. De Jong, J.W. Geus, Catal. Rev. Sci. Eng. 42 (2000) 481.
[38] F. Cesano, S. Bertarione, D. Scarano, et al., Chem. Mater. 17 (2005) 5119.
[39] J. Robertson, Mater. Sci. Eng. R: Rep. 37 (2002) 129.
[40] G. Zerbi, M. Tommasini, A. Centrone, et al., A Spectroscopic Approach to Carbon Materials for Energy Storage. Carbon: The Future Material for Advanced Technology Applications, Springer-Verlag, Berlin, 2006, p. 23.
[41] J.M. Calleja, M. Cardona, Phys. Rev. B 16 (1977) 3753.
[42] C.X. Xu, X.W. Sun, Z.L. Dong, et al., Appl. Phys. Lett. 85 (2004) 3878.
[43] X.T. Zhang, Y.C. Liu, Z.Z. Zhi, et al., J. Phys. D: Appl. Phys. 34 (2001) 3430.
[44] M. Tzolov, N. Tzenov, D. Dimova-Malinovska, et al., Thin Solid Films 379 (2000) 28.
[45] S.Y. Bae, H.W. Seo, H.C. Choi, et al., J. Phys. Chem. B 108 (2004) 12318.
[46] C. Li, G. Xiong, Q. Xin, et al., Angew. Chem. Int. Ed. 38 (1999) 2220.
[47] G. Ricchiardi, A. Damin, S. Bordiga, et al., J. Am. Chem. Soc. 123 (2001) 11409.
[48] S. Bordiga, A. Damin, F. Bonino, et al., Angew. Chem. Int. Ed. 41 (2002) 4734.
[49] S. Bordiga, A. Damin, F. Bonino, et al., Phys. Chem. Chem. Phys. 5 (2003) 4390.
[50] A. Damin, F.X.L. Xamena, C. Lamberti, et al., J. Phys. Chem. B 108 (2004) 1328.
[51] S. Usseglio, P. Calza, A. Damin, et al., Chem. Mater. 18 (2006) 3412.
[52] E. Groppo, A. Damin, F. Bonino, et al., Chem. Mater. 17 (2005) 2019.
[53] A. Damin, F. Bonino, S. Bordiga, et al., Chemphyschem 7 (2006) 342.
[54] S. Bordiga, C. Lamberti, G. Ricchiardi, et al., Chem. Commun. (2004) 2300.
[55] M.J. Matthews, M.A. Pimenta, G. Dresselhaus, et al., Phys. Rev. B 59 (1999) R6585.
[56] I. Pocsik, M. Hundhausen, M. Koos, et al., J. Non-Cryst. Solids 230 (1998) 1083.
[57] G.I. Dovbeshko, O.P. Gnatyuk, A.N. Nazarova, et al., Fulleren. Nanotubes Carbon Nanostruct. 13 (2005) 393.
[58] Z. Wang, S. Li, Y. Lu, et al., Preparation, characterization, and optical properties of carbon doped ZnO nanocrystal, in: W.L.A.J. Young (Ed.), Proceedings of SPIE Materials and Nanostructures, 2006, p. 60290R.
[59] Y. Imai, A. Watanabe, J. Mater. Sci.: Mater. Electron. 15 (2004) 743.